

Detection of standing internal gravity waves in experiments with convection over a wavy heated wall

L. Barel,^{*} A. Eidelman,[†] T. Elperin, G. Fleurov,[‡] N. Kleeorin,[§] A. Levy,[¶] and I. Rogachevskii^{**}

The Pearlstone Center for Aeronautical Engineering Studies, Department of Mechanical Engineering, Ben-Gurion University of the Negev, P.O.Box 653, Beer-Sheva 84105, Israel

(Dated: February 14, 2019)

Convection over a wavy heated bottom wall in the air flow has been studied in the experiments with the Rayleigh number $\sim 10^8$. It is shown that the mean temperature gradient in the flow core inside the large-scale circulation is directed upward, that corresponds to the stably stratified flow. In this experiments with a wavy heated bottom wall, we detect large-scale standing internal gravity waves excited in the regions with the stably stratified flow. The wavelength and the period of these waves are much larger than the turbulent spatial and time scales, respectively. In particular, the frequencies of the observed large-scale waves vary from 0.01 Hz to 0.1 Hz, while the turbulent time in the integral scale is about 0.5 s. The measured spectrum of these waves contains several localized maxima, that implies an existence of waveguide resonators for the internal gravity waves. For the same imposed mean temperature differences between bottom and upper walls, but in the experiments with a smooth plane bottom wall, there are much less locations with a stably stratified flow, and the internal gravity waves are not observed.

I. INTRODUCTION

Temperature stratified turbulence in convective and stably stratified flows has been investigated theoretically, experimentally and in numerical simulations due to numerous applications in geophysical, astrophysical and industrial flows (see, e.g., [1–10]). One of the key ingredients of stably stratified flows are internal gravity waves. In atmospheric and oceanic turbulence they have been a subject of intense research (see, e.g., [11–29]). In the atmosphere, internal gravity waves exist at scales ranging from meters to kilometers, and are measured by direct probing or remote sensing using radars and lidars [17, 24]. The sources of internal gravity waves can be flows over complex terrain, strong wind shears, convective and other local-scale motions underlying the stably stratified layer, and wave-wave interactions [17, 18]. The internal gravity waves propagation is complicated by variable wind and density profiles causing refraction, reflection, focusing, and ducting.

The internal gravity waves can strongly affect the small-scale turbulence. In particular, these waves create additional productions of turbulent energy and additional vertical turbulent fluxes of momentum and heat. In particular, the waves emitted at a certain level, propagate upward, and the losses of wave energy cause the production of turbulence energy. These effects have been studied theoretically in [30, 31], where the energy- and flux-budget (EFB) turbulence closure theory which accounts for large-scale internal gravity waves (IGW) for

stably stratified atmospheric flows has been developed. For the stationary (in statistical sense) and homogeneous turbulence, the EFB theory without large-scale IGW [32–35] yields universal dependencies of the main turbulence parameters on the flux Richardson number (defined as the ratio of the consumption of turbulent kinetic energy (TKE) needed for overtaking buoyancy forces to the TKE production by the velocity shear). Due to the large-scale IGW, these dependencies lose their universality [30, 31]. The maximum value of the flux Richardson number (universal constant ≈ 0.25 in the absence of the large-scale IGW) becomes strongly variable. In the vertically homogeneous stratification, the flux Richardson number increases with increasing wave energy and can even exceed 1. For heterogeneous stratification, when internal gravity waves propagate towards stronger stratification, the maximal flux Richardson number decreases with increasing wave energy and even can reach very small values [30, 31].

Internal gravity waves also reduce the anisotropy of turbulence: in contrast to the mean wind shear, which generates only horizontal TKE, internal gravity waves generate both horizontal and vertical TKE. A well-known effect of internal gravity waves is their direct contribution to the vertical transport of momentum. Depending on the direction of the wave propagation (downward or upward), the internal gravity waves either strengthen or weaken the total vertical flux of momentum [30, 31].

Even in a convective turbulence, stably stratified regions can be formed, where the mean temperature gradient in the flow core inside the large-scale circulation is directed upward [36, 37]. In these regions internal gravity waves are generated, which affect the turbulence. In spite of many studies of stratified turbulence and internal gravity waves, a mechanism of formation of the stably stratified regions in convective turbulence, and generation of internal gravity waves in these regions is not comprehensively studied and understood.

^{*} lielba@post.bgu.ac.il

[†] eidel@bgu.ac.il

[‡] gabrief@gmail.com

[§] nat@bgu.ac.il

[¶] avi@bgu.ac.il

^{**} gary@bgu.ac.il

In various flows a complex terrain (i.e., canopy and various topography) strongly affects the stratified turbulence [38]. It changes local temperature gradients, heat and mass fluxes, and affects a local structure of fluid flows. Therefore, one of the important questions — what is the effect of complex terrain on convective and stably stratified turbulence?

To model the effect of complex terrain, the Rayleigh-Bénard convection (RBC) with modulated boundaries has been investigated in [36, 39–45]. In particular, the influence of a modulated boundary on RBC by a lithographically fabricated periodic texture on the bottom plate has been studied experimentally in [42]. The different convection patterns have been obtained by varying the Rayleigh number and the wave number of the modulated boundary. For small Rayleigh numbers, convection takes the form of straight parallel rolls. With increasing Rayleigh number, a secondary instability is excited and the convection has more complex patterns [42]. This secondary instability has been studied theoretically and numerically in [43].

The roughness effect on the heat transport in RBC has been investigated in two-dimensional numerical simulations in [36, 44] by varying the height and wavelength of the roughness elements. The sinusoidal roughness profile has been chosen in [36, 44]. The ultimate regime of thermal convection (when the boundary layers undergo a transition leading to the generation of smaller scales near the boundaries that increase the systems efficiency in transporting the heat) has been found in [36]. This regime in which the heat flux becomes independent of the molecular properties of the fluid, has been predicted in [47] (see also [48]). The first experiment designed to use roughness to reach the ultimate regime at accessible Rayleigh numbers has been made in [45]. One of the key role of the roughness elements is the production and release of the plumes from the roughness elements, resulting formation of larger plumes. This can cause an increase in the efficiency of the heat transfer [36, 46]. The existence of two universal regimes in RBC, namely the ultimate regime and the classical boundary-layer-controlled regime with increased Rayleigh number, have been demonstrated in [44]. The transition from the first to the second regime is determined by the competition between bulk and boundary layer flow. The bulk-dominated regime corresponds to the ultimate regime.

In the present study, we investigate another aspects related to effects of complex terrain on turbulent convection. In particular, we study formation of the stably stratified regions and excitation of internal gravity waves in laboratory experiments with turbulent convection over a wavy heated bottom wall in the air as the working fluid. An interactions of the large-scale convective circulation with a wavy heated bottom wall strongly modifies the mean temperature spatial distribution producing stably stratified regions in the flow core, and causes generation of large-scale standing internal gravity waves. The measured spectrum of the waves contains several local-

ized maxima, that indicates an existence of the waveguide resonators of the internal gravity waves in the stably stratified regions. We have compared the results of these experiments for the same imposed mean temperature differences between bottom and upper walls with those obtained in the experiments with a smooth plane bottom wall.

This paper is organized as follows. In Section II we determine the frequencies of the standing internal gravity waves in stably stratified flow. In Section III we describe the experimental set-up and instrumentation. The results of laboratory study and comparison with the theoretical predictions are presented in Section IV. Finally, conclusions are drawn in Section V.

II. INTERNAL GRAVITY WAVES

Let us first consider the internal gravity waves propagating in a stably stratified fluid in the absence of turbulence and neglecting dissipations. These waves are described by the following momentum and entropy equations written in the Boussinesq approximation:

$$\frac{\partial \mathbf{V}^W}{\partial t} + (\mathbf{V}^W \cdot \nabla) \mathbf{V}^W = -\frac{\nabla P^W}{\rho} + g S^W \mathbf{e}, \quad (1)$$

$$\frac{\partial S^W}{\partial t} + (\mathbf{V}^W \cdot \nabla) S^W = -g^{-1} N^2 V_j^W e_j, \quad (2)$$

(see, e.g., [1, 13–15]), where \mathbf{V}^W , S^W and P^W are the velocity, entropy and pressure, respectively, which are caused by the internal gravity waves, \mathbf{e} is the vertical unit vector, \mathbf{g} is the acceleration due to gravity, $N(z) = (g \nabla_z S)^{1/2}$ is the Brunt-Väisälä frequency, ρ and S are the density and entropy of fluid, respectively. The entropy is defined as $S = c_v \ln(P \rho^{-\gamma})$ and we use the equation of state for the perfect gas, where T and P are the fluid temperature and pressure, and $\gamma = c_p/c_v$ is the ratio of the specific heats, c_p and c_v , at constant pressure and volume, respectively. The Boussinesq approximation with $\text{div } \mathbf{V}^W = 0$ is applied here.

Linearised Eqs. (1) and (2) yield the frequency ω of the internal gravity waves:

$$\omega = N(z) \frac{k_h}{k}, \quad (3)$$

where $\mathbf{k} = \mathbf{k}_h + e k_z$ is the wave vector and $\mathbf{k}_h = (k_x, k_y)$ is the wave vector in the horizontal direction. Propagation of the internal gravity waves in the stably stratified flow in the approximation of geometrical optics is determined by the following Hamiltonian equations:

$$\frac{\partial \mathbf{r}}{\partial t} = \frac{\partial \omega}{\partial \mathbf{k}}, \quad (4)$$

$$\frac{\partial \mathbf{k}}{\partial t} = -\frac{\partial \omega}{\partial \mathbf{r}}, \quad (5)$$

(see, e.g., [49]), where \mathbf{r} is the radius-vector of the centre of the wave packet. Since the Brunt-Väisälä frequency $N = N(z)$, the only non-zero spatial derivative,

$\nabla_z \omega \neq 0$, is in the vertical direction. Therefore, Eq. (5) yields $\mathbf{k}_h = \text{const.}$ The vertical component of the wave vector $k_z = k_z(z)$ is determined from Eq. (3):

$$k_z(z) = k_h \left(\frac{N^2(z)}{\omega^2} - 1 \right)^{1/2}. \quad (6)$$

Taking twice **curl** to exclude the pressure term in linearised Eq. (1), calculating the time derivative of the obtained equation and using linearised Eq. (2), we arrive at the following equation:

$$\frac{\partial^2}{\partial t^2} \Delta \mathbf{V}^W = [\nabla(\mathbf{e} \cdot \nabla) - \mathbf{e}\Delta] V_z^W N^2(z), \quad (7)$$

which is equivalent to the system of equations for the vertical and horizontal velocity components:

$$\frac{\partial^2}{\partial t^2} \Delta V_z^W = -N^2(z) \Delta_{\perp} V_z^W, \quad (8)$$

$$\frac{\partial^2}{\partial t^2} \Delta \mathbf{V}_{\perp}^W = \nabla_{\perp} \Delta_z [V_z^W N^2(z)]. \quad (9)$$

Here $\mathbf{V}^W = \mathbf{V}_{\perp}^W + \mathbf{e}V_z^W$, $\mathbf{V}_{\perp}^W = (V_x^W, V_y^W)$ is the horizontal velocity for IGW and $\Delta = \Delta_{\perp} + \Delta_z$. Solution of Eq. (8) for $V_z^W(t, \mathbf{r})$ we seek for in the form of standing internal gravity waves existing in the range $z_{\min} \leq z \leq z_{\max}$:

$$V_z^W(t, \mathbf{r}) = V_* \cos(\omega t) \cos(\mathbf{k}_h \cdot \mathbf{r}) \times \sin \left(\int_{z_{\min}}^z k_z(z') dz' + \varphi \right). \quad (10)$$

Substituting Eq. (10) into Eq. (9), we obtain solution for the horizontal velocity $\mathbf{V}_{\perp}^W(t, \mathbf{r})$:

$$\mathbf{V}_{\perp}^W(t, \mathbf{r}) = -\mathbf{k}_h \frac{k_z(z)}{k_h^2} V_* \cos(\omega t) \sin(\mathbf{k}_h \cdot \mathbf{r}) \times \cos \left(\int_{z_{\min}}^z k_z(z') dz' + \varphi \right). \quad (11)$$

Using Eqs. (2) and (10), we obtain solution for $S^W(t, \mathbf{r})$:

$$S^W(t, \mathbf{r}) = \frac{N^2(z)}{g\omega} V_* \sin(\omega t) \cos(\mathbf{k}_h \cdot \mathbf{r}) \times \sin \left(\int_{z_{\min}}^z k_z(z') dz' + \varphi \right). \quad (12)$$

The solution (10) should satisfy the following boundary conditions: $V_z^W(z = z_{\min}) = 0$ and $V_z^W(z \approx z_{\max}) = 0$. The boundary condition, $V_z^W(z \approx z_{\max}) = 0$, at the vicinity $z \approx z_{\max}$ implies that

$$\int_{z_{\min}}^{z_{\max}} k_z(z') dz' = \pi \left(m + \frac{1}{4} \right), \quad (13)$$

where z_{\max} is the reflection (or "turning") point in which $k_z(z = z_{\max}) = 0$. To get the condition (13), we use an analogy between this problem and the quantum mechanics problem that is related to the behavior of the wave function near the turning points in the semi-classical

limit [50]. The wave functions are described in terms of the Airy functions, and Eq. (13) is analogous to the Bohr-Sommerfeld quantization condition. In particular, the phase φ in Eq. (11) is determined using asymptotics [$\propto \sin(\int_{z_{\min}}^z k_z(z') dz' + \pi/4)$] for the Airy function in the vicinity of $z \approx z_{\max}$.

Equation (13) yields the frequencies of the standing internal gravity waves for the quadratic profile of the Brunt-Väisälä frequency $N^2(z) = N_0^2(1 - z^2/L_N^2)$:

$$\omega_m = \frac{N_0}{k_h L_N} \left\{ \left[\left(m + \frac{1}{4} \right)^2 + (k_h L_N)^2 \right]^{1/2} - \left(m + \frac{1}{4} \right) \right\}, \quad (14)$$

where $m = 0, 1, 2, \dots$ Equation (14) implies the existence of a discrete spectrum of the standing internal gravity waves. In the long wavelength limit, $k_h L_N \ll 1$, Eq. (14) yields

$$\omega_m = \frac{2N_0}{4m+1} k_h L_N. \quad (15)$$

We will use Eq. (14) in the experimental study of convection over a wavy heated bottom wall, where the large-scale internal gravity waves are excited in the stably stratified regions formed inside the flow core of the large-scale circulation.

III. EXPERIMENTAL SET-UP

In this section we describe the experimental set-up. The experiments have been conducted in air as the working fluid in rectangular chamber with dimensions $L_x \times L_y \times L_z$, where $L_x = L_z = 26$ cm, $L_y = 58$ cm and the axis z is in the vertical direction. The side walls of the chamber are made of transparent Perspex with the thickness of 1 cm.

A vertical mean temperature gradient in the turbulent air flow is formed by attaching two aluminium heat exchangers to the bottom and top walls of the test section (a heated bottom and a cooled top wall of the chamber). The temperature difference between the top and bottom plates, ΔT , in the experiments are from 40 K to 70 K. The top plate is a bottom wall of the tank with cooling water. Temperature of water circulating through the tank and the chiller is kept constant within 0.1 K. Cold water is pumped into the cooling system through two inlets and flows out through two outlets located at the side wall of the cooling system.

We study the effects of complex terrain on the structure of the velocity and temperature fields in stratified turbulence. In the laboratory experiments complex terrain is modelled by a wavy bottom wall of the chamber which is manufactured from aluminium. The wavy bottom wall has a sinusoidal modulation containing 7 periods with wavelength 7.8 cm and amplitude 1 cm. A sketch of the experimental set-up is shown in Fig. 1. The

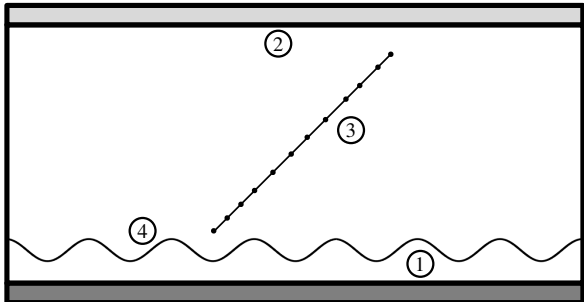


FIG. 1. A sketch of the experimental set-up: heat exchangers at the bottom (1) and top (2) walls; temperature probe (3) equipped with 12 E-thermocouples; a wavy bottom wall (4) with a sinusoidal modulation.

results of these experiments for the same imposed mean temperature differences between bottom and upper walls are compared with those obtained in the experimental set-up with a smooth plane bottom wall.

The temperature field is measured with a temperature probe equipped with 12 E-thermocouples (with the diameter of 0.13 mm and the sensitivity of $\approx 65 \mu\text{V/K}$) attached to a rod with a diameter 4 mm. The spacing between thermocouples along the rod is 22 mm. Each thermocouple is inserted into a 1 mm diameter and 45 mm long case. A tip of a thermocouple protruded at the length of 15 mm out of the case. The temperature is measured for 11 rod positions with 22 mm intervals in the horizontal direction, i.e., at 121 locations in a flow. Due to space constraints, the probe is positioned at a 45 degree angle. The exact position of each thermocouple is measured using images captured with the optical system employed in Particle Image Velocimetry (PIV) measurements. A sequence of 500 temperature readings for every thermocouple at every rod position is recorded and processed.

The velocity field is measured using a Stereoscopic Particle Image Velocimetry, see Refs. [51–53]. In the experiments we use LaVision Flow Master III system. A double-pulsed light sheet is provided by a Nd-YAG laser (Continuum Surelite 2×170 mJ). The light sheet optics includes spherical and cylindrical Galilei telescopes with tuneable divergence and adjustable focus length. We use the progressive-scan 12 bit digital CCD camera (with pixel size $6.7 \mu\text{m} \times 6.7 \mu\text{m}$ and 1280×1024 pixels) with a dual-frame-technique for cross-correlation processing of captured images. A programmable Timing Unit (PC interface card) generated sequences of pulses to control the laser, camera and data acquisition rate.

An incense smoke with sub-micron particles is used as a tracer for the PIV measurements. Smoke is produced by high temperature sublimation of solid incense grains. Analysis of smoke particles using a microscope (Nikon, Epiphot with an amplification of 560) and a PM-

300 portable laser particulate analyzer shows that these particles have an approximately spherical shape and that their mean diameter is of the order of $0.7 \mu\text{m}$. The maximum tracer particle displacement in the experiment is of the order of 1/4 of the interrogation window. The average displacement of tracer particles is of the order of 2.5 pixels. The average accuracy of the velocity measurements is of the order of 4% for the accuracy of the correlation peak detection in the interrogation window of the order of 0.1 pixel (see, e.g., Refs. [51–53]).

We determine the mean and the r.m.s. velocities, two-point correlation functions and an integral scale of turbulence from the measured velocity fields. Series of 520 pairs of images acquired with a frequency of 2 Hz, are stored for calculating velocity maps and for ensemble and spatial averaging of turbulence characteristics. The center of the measurement region coincides with the center of the chamber. We measure velocity in a flow domain $256 \times 503 \text{ mm}^2$ with a spatial resolution of $393 \mu\text{m} / \text{pixel}$. The velocity field in the probed region is analyzed with interrogation windows of 32×32 pixels. In every interrogation window a velocity vector is determined from which velocity maps comprising 27×53 vectors are constructed. The mean and r.m.s. velocities for every point of a velocity map are calculated by averaging over 520 independent velocity maps, and the obtained averaged velocity map is averaged also over the central flow region.

The two-point correlation functions of the velocity field are determined for every point of the central part of the velocity map (with 16×16 vectors) by averaging over 520 independent velocity maps, which yields 16 correlation functions in horizontal and vertical directions. The two-point correlation function is obtained by averaging over the ensemble of these correlation functions. An integral scale of turbulence, ℓ , is determined from the two-point correlation functions of the velocity field. The turbulence time scale at the integral scale is $\tau = \ell / \sqrt{\langle \mathbf{u}^2 \rangle}$, where \mathbf{u} are the velocity fluctuations and $\sqrt{\langle \mathbf{u}^2 \rangle}$ is the r.m.s. of the velocity fluctuations. In the experiments we evaluated the variability between the first and the last 20 velocity maps of the series of the measured velocity field. Since very small variability is found, these tests show that 520 velocity maps contain enough data to obtain reliable statistical estimates. The size of the probed region does not affect our results.

In our study we employ a triple decomposition whereby the instantaneous temperature $T^{\text{tot}} = T + \theta$, where θ are the temperature fluctuations and T is the temperature determined by sliding averaging of the instantaneous temperature field over the time that is by one order of magnitude larger than the characteristic turbulence time. This temperature T is given by a sum, $T = \bar{T} + T^{\text{W}}$, where T^{W} are the long-term variations of the temperature T due to the large-scale standing internal gravity waves around the mean value \bar{T} . The mean temperature \bar{T} is obtained by the additional averaging of the temperature T over the time 400 s.

The time interval during which temperature field is

measured at every point, is 400 s, which corresponds to 500 data points of the temperature field (over which we perform averaging). In the temperature measurements, the acquisition frequency of the temperature is 1.25 Hz, and the corresponding acquisition time is 0.8 s. It is larger than the characteristic turbulence time (see below), and is much smaller than the period of the long-term oscillations of the mean temperature caused by internal gravity waves. Therefore, the acquisition frequency of temperature is high enough to provide sufficiently long time series for statistical estimation of the mean temperature \bar{T} and the long-term variations T^W of the temperature due to the large-scale internal gravity waves. Similar experimental set-ups, measurement techniques for temperature and velocity fields and data processing procedures have been used previously in our experimental study of different aspects of turbulent convection [54, 55] and stably stratified turbulence [56, 57].

IV. EXPERIMENTAL RESULTS

In this section we describe experimental results related to formation of stably stratified regions in turbulent convection and excitation of internal gravity waves. We perform two sets of experiments with (i) a wavy bottom wall and (ii) a smooth plane bottom wall for the same imposed mean temperature differences ΔT between bottom and upper walls. The velocity measurements show that in the both sets of experiments, a one large-scale circulation is observed for the temperature differences $\Delta T = 40$ K and $\Delta T = 50$ K. In this section we present all results only for these values of ΔT . In Fig. 2 we show the mean velocity patterns obtained in the experiments with the wavy bottom wall (upper panel) and smooth plane bottom wall (bottom panel). A difference in the mean velocity patterns is clearly seen at the vicinity of the wavy bottom wall where the flows with the sinusoidal modulation of the mean velocity field are observed (see upper panel in Fig. 2). Other comparison of the results obtained in these two sets of experiments is discussed in the second part of this section.

Now we discuss parameters in the experiments with the wavy bottom wall. The characteristic turbulence time is $\tau = 0.28 - 0.62$ seconds, while the characteristic period for the large-scale circulatory flow is about 10 s, which is by order of magnitude larger than τ . These two characteristic times are much smaller than the time during which the velocity fields are measured (~ 260 s). The maximum Rayleigh number, $Ra = \alpha g L_z^3 \Delta T / (\nu \kappa)$, is about 10^8 , where α is the thermal expansion coefficient, ν is the kinematic viscosity, κ is the thermal diffusivity, and L_z in the experiments with a wavy bottom wall is the height measured from the lower point of a wavy wall with sinusoidal modulation to the upper wall of the chamber.

The temperature measurements in the experiments with a wavy bottom wall, show that the mean temperature gradient in the flow core ($193 \text{ mm} \leq y \leq 333 \text{ mm}$, 40

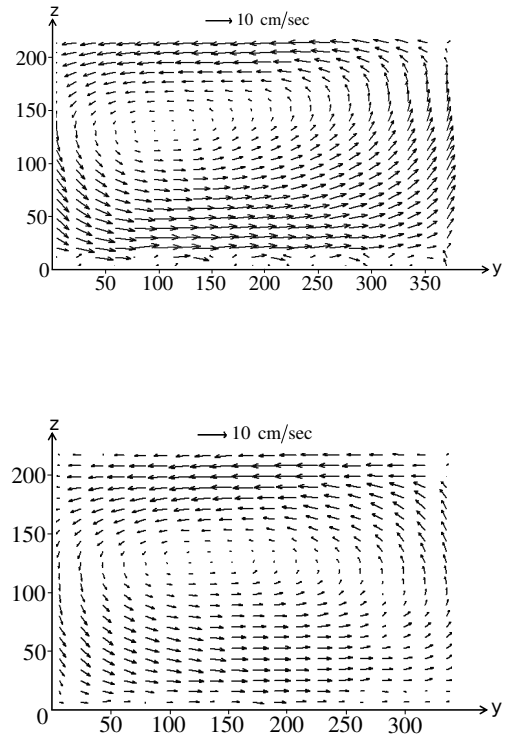


FIG. 2. The mean velocity patterns for the experiments with the wavy bottom wall (upper panel) and the smooth plane bottom wall (bottom panel) obtained at $\Delta T = 50$ K. Here the z and y are measured in mm.

$\text{mm} \leq z \leq 180 \text{ mm}$) inside the large-scale circulation is directed upward, that corresponds to the stably stratified flow. We have measured the temperature field in this region in 80 locations. In Fig. 3 we show profiles of the vertical mean temperature gradient $\nabla_z \bar{T}$ in the experiments for different temperature differences ΔT between the bottom and top walls. These profiles of the vertical mean temperature gradient are also averaged over y -coordinate in the core flow ($193 \text{ mm} \leq y \leq 333 \text{ mm}$) of the large-scale circulation. In particular, they are averaged over 8 vertical profiles measured at 8 equidistant positions located in the y direction with the interval $\Delta y = 20 \text{ mm}$ between the temperature probes.

There are two maxima of the mean temperature gradient separated by one minimum in the center of the core flow (see Fig. 3). At the minimum of $\nabla_z \bar{T}$, the mean temperature gradient is positive for the dashed curve (corresponding to the experiments with $\Delta T = 40$ K), and the minimum of $\nabla_z \bar{T}$ tends to very small negative value for the solid curve (for the experiments with $\Delta T = 50$ K). In the case of negative vertical mean temperature gradient $\nabla_z \bar{T}$, the value of $N^2 < 0$ and the internal gravity waves cannot exist in the vicinity of this region. This means that for $\Delta T = 50$ K, there are two waveguides for the internal gravity waves, while in the first case ($\Delta T = 40$ K) there is only one waveguide. In these experiments the

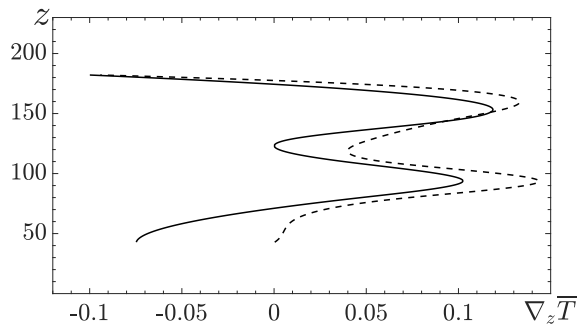


FIG. 3. Profiles of the vertical mean temperature gradient $\nabla_z \bar{T}$ in the experiments for different temperature differences ΔT between the bottom and top walls: 40 K (dashed) and 50 K (solid). Here the height z is measured in mm, and the mean temperature gradient is measured in K/cm.

maximum gradient Richardson number, $Ri = N^2/Sh^2$, based on the mean velocity shear, Sh , of the large-scale circulation is about 1. Here N is the Brunt-Väisälä frequency.

To study internal gravity waves, we determine spectrum of the long-term variations of the temperature field characterising the large-scale IGW. From this spectral analysis we obtain main frequencies of IGW. The spectrum function $E_T(f) = \tilde{T}(f) \tilde{T}^*(f)$ for the temperature field (containing 250 frequency data points) has been determined at 80 locations of the stably stratified region, where the temperature $\tilde{T}(t) = T^{\text{tot}} - \bar{T}$ and $\tilde{T}(f)$ is its Fourier component. For every frequency f , the obtained spectrum functions $E_T(f)$ have been averaged over 80 locations. In Figs. 4 and 5 we show the averaged spectrum function $E_{\tilde{T}}(f)$ of the temperature field in the experiments for the temperature differences $\Delta T = 50$ K and $\Delta T = 40$ K, respectively.

Comparing the main frequencies of internal gravity waves obtained in the temperature measurements with the profile of the Brunt-Väisälä frequency (based on the measured profile of the mean temperature gradient), we determine the horizontal wave-numbers for the observed internal gravity waves. Figures 6 and 7 show the theoretical dependencies for the frequencies of the internal gravity waves versus the normalized horizontal wavelength λ_h/L_N given by Eq. (14), where L_N is the characteristic vertical scale of the Brunt-Väisälä frequency variations and $\lambda_h = 2\pi/k_h$ is the horizontal wavelength. The theoretical curves are plotted for the first three main modes of the large-scale IGW.

Using the theoretical curves and the measured frequencies of the long-term variations of the temperature fields in the experiments with the temperature differences $\Delta T = 50$ K (Fig. 6) and $\Delta T = 40$ K (Fig. 7), we determine the horizontal wavelengths associated with different modes of the large-scale IGW. Note that in the experiments where there is only a one waveguide, it is possible to observe two dominant modes. For instance,

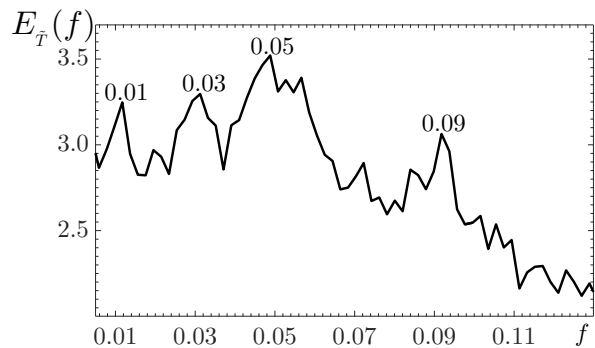


FIG. 4. The averaged spectrum function $E_{\tilde{T}}(f)$ of the temperature field obtained in the experiments for the temperature differences $\Delta T = 50$ K between the bottom and top walls. The main frequencies of the large-scale IGW measured in Hz are indicated above the maxima of \tilde{T} . The function $\tilde{T}(f)$ is measured in K^2/Hz .

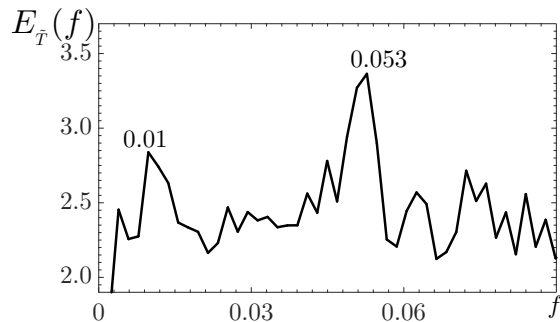


FIG. 5. The averaged spectrum function $E_{\tilde{T}}(f)$ of the temperature field obtained in the experiments for the temperature differences $\Delta T = 40$ K between the bottom and top walls. The main frequencies of the large-scale IGW measured in Hz are indicated above the maxima of \tilde{T} . The function $\tilde{T}(f)$ is measured in K^2/Hz .

in the case of two waveguides for the large-scale IGW, we observe four wave frequencies (two in the each waveguide), see Fig. 6. On the other hand, in the experiments with $\Delta T = 40$ K where there is only one waveguide, we observe two frequencies of large-scale standing internal gravity waves (see Fig. 7).

To compare the results for the two sets of experiments with the wavy and smooth plane bottom walls, conducted at the same imposed mean temperature differences between bottom and upper walls, we show in Fig. 8 the vertical profiles of the rms velocity components $u_y^{\text{rms}} = \sqrt{\langle u_y^2 \rangle}$ and $u_z^{\text{rms}} = \sqrt{\langle u_z^2 \rangle}$. In particular, in the experiments with the wavy bottom wall, there is a minimum in the vertical profiles of the rms velocities in the center part of the chamber. This minimum may be caused by the presence of stably stratified turbulence in the center part of the chamber where the intensity of the

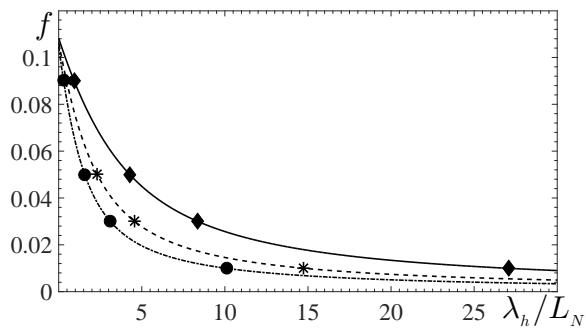


FIG. 6. The frequencies of the internal gravity waves (measured in Hz) versus the normalized horizontal wavelength λ_h/L_N : theoretical curves for different modes $m = 1$ (solid), $m = 2$ (dashed) and $m = 3$ (dashed-dotted) and measured frequencies associated with different modes: $m = 1$ (diamonds), $m = 2$ (snowflakes) and $m = 3$ (circles) in the experiments for the temperature differences $\Delta T = 50$ K between the bottom and top walls.

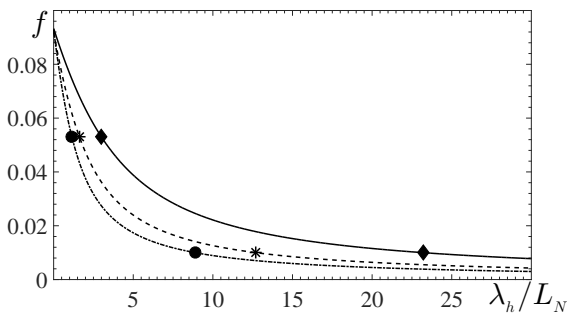


FIG. 7. The frequencies of the internal gravity waves (measured in Hz) versus the normalized horizontal wavelength λ_h/L_N : theoretical curves for different modes $m = 1$ (solid), $m = 2$ (dashed) and $m = 3$ (dashed-dotted) and measured frequencies associated with different modes: $m = 1$ (diamonds), $m = 2$ (snowflakes) and $m = 3$ (circles) in the experiments for the temperature differences $\Delta T = 40$ K between the bottom and top walls.

velocity fluctuations are partially depleted by the production of the temperature fluctuations. On the other hand, in the experiments with the smooth plane bottom wall, the vertical distribution of the rms velocities is essentially less inhomogeneous.

In the mean temperature field we observe much more differences for these two kind of experiments. In particular, in the experiments with a smooth plane bottom wall there are much less locations with positive mean temperature gradient (corresponding to the stably stratified flows) and internal gravity waves are not observed there.

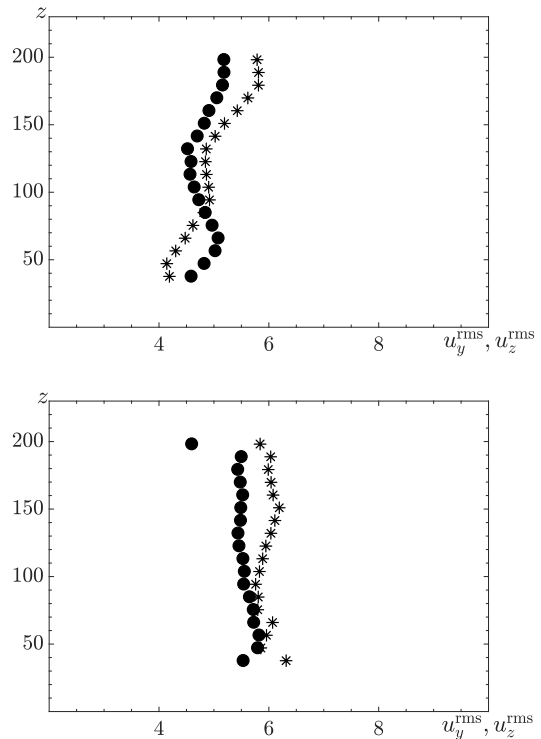


FIG. 8. The vertical profiles of the rms velocities u_y^{rms} (stars) and u_z^{rms} (circles) in the experiments with the wavy bottom wall (upper panel) and the smooth plane bottom wall (bottom panel) obtained at $\Delta T = 50$ K. Here the z is measured in mm, and the rms velocities u_y^{rms} and u_z^{rms} are measured in cm/s.

V. CONCLUSIONS

In the present study we perform laboratory experiments in convection over a wavy heated bottom wall. An interaction of the large-scale circulation with the wavy heated bottom wall strongly affects the spatial structure of the mean temperature field in the flow core. In particular, we have found that there are many locations with stably stratified regions in the flow core of the large-scale circulation, and the large-scale standing internal gravity waves are excited in these regions. The spectrum of these waves contains several localized maxima, that is an indication of existence of the waveguide resonators for the internal gravity waves. The theoretical predictions are in an agreement with the obtained experimental results. On the other hand, in the experiments with a smooth plane bottom wall but the same imposed mean temperature differences between bottom and upper walls, there are much less locations with a stably stratified turbulence and the internal gravity waves are not detected. The turbulence in the region with stably stratified flows in the experiments with the wavy bottom wall is inhomogeneous, e.g., there is a minimum in the vertical profiles of the rms velocities in the center part of the chamber, where the intensity of the velocity fluctuations are partially de-

pleted by the production of the temperature fluctuations. On the other hand, in the experiments with the smooth plane bottom wall, the vertical distribution of the rms velocities is nearly homogeneous.

ACKNOWLEDGMENTS

We thank A. Krein for his assistance in construction of the experimental set-up. The detailed comments on our manuscript by the two anonymous referees which essentially improved the presentation of our results, are very much appreciated. This research was supported in part by the Israel Science Foundation governed by the Israel Academy of Sciences (grant No. 1210/15).

-
- [1] J. S. Turner, *Buoyancy Effects in Fluids* (Cambridge University Press, Cambridge, 1973).
- [2] A. S. Monin and A. M. Yaglom, *Statistical Fluid Mechanics* (MIT Press, Cambridge, Massachusetts, 1975), Vol. 2.
- [3] J. C. Kaimal and J. J. Finnigan, *Atmospheric Boundary Layer Flows* (Oxford University Press, New York, 1994).
- [4] S. S. Zilitinkevich, *Turbulent Penetrative Convection* (Avebury Technical, Aldershot, 1991).
- [5] J. R. Garratt, *The Atmospheric Boundary Layer* (Cambridge University Press, Cambridge 1992).
- [6] S. V. Nazarenko, *Wave Turbulence*, Lecture Notes in Physics, vol. 825 (Springer, Heidelberg, 2011).
- [7] E. S. C. Ching, *Statistics and Scaling in Turbulent Rayleigh-Bnard Convection* (Springer, Singapore, 2014).
- [8] G. Ahlers, S. Grossmann, D. Lohse, *Rev. Mod. Phys.* **81**, 503 (2009).
- [9] D. Lohse, K.-Q. Xia, *Annu. Rev. Fluid Mech.* **42**, 335 (2010).
- [10] F. Chillà, J. Schumacher, *Eur. Phys. J. E* **35**, 58 (2012).
- [11] T. Beer, *Atmospheric Waves* (Wiley, New York, 1974).
- [12] E. E. Gossard and W. H. Hooke, *Waves in the Atmosphere* (Elsevier, New York, 1975).
- [13] Yu. Z. Miropol'sky, *Dynamics of Internal Gravity Waves in the Ocean* (Springer, Dordrecht, 2001).
- [14] C. J. Nappo, *An Introduction to Atmospheric Gravity Waves*, (Academic Press, London, 2002).
- [15] B. R. Sutherland, *Internal Gravity Waves* (Cambridge Univ. Press, Cambridge, 2010).
- [16] C. Garrett and W. Munk, *Annu. Rev. Fluid Mech.* **11**, 339 (1979).
- [17] D. C. Fritts and M. J. Alexander, *Rev. Geophys.* **41**, 1003 (2003).
- [18] C. Staquet and J. Sommeria, *Annu. Rev. Fluid Mech.* **34**, 559 (2002).
- [19] J. J. Finnigan and F. Einaudi, *Quart. J. Roy. Met. Soc.* **107**, 807 (1981).
- [20] J. J. Finnigan, F. Einaudi and D. Fua, *J. Atmosph. Sci.* **41**, 2409 (1984).
- [21] F. Einaudi, J. J. Finnigan and D. Fua, *J. Atmosph. Sci.* **41**, 661 (1984).
- [22] J. J. Finnigan, *J. Atmosph. Sci.* **45**, 486 (1988); *Boundary-Layer Meteorol.* **90**, 529 (1999).
- [23] F. Einaudi and J. J. Finnigan, *J. Atmosph. Sci.* **50**, 1841 (1993).
- [24] G. Chimonas, *Boundary-Layer Meteorol.* **90**, 397 (1999).
- [25] S. S. Zilitinkevich, *Quart. J. Roy. Met. Soc.* **128**, 913 (2002).
- [26] L. H. Jin, R. M. C. So and T. B. Gatski, *J. Fluid Mech.* **482**, 207 (2003).
- [27] H. Baumert and H. Peters, *J. Phys. Oceanogr.* **34**, 505 (2004); *Ocean Sci.* **5**, 47 (2009).
- [28] F. G. Jacobitz, M. M. Rogers and J. H. Ferziger, *J. Turbulence* **6**, 1 (2005).
- [29] J. Sun, C. J. Nappo, L. Mahrt, D. Belusic, B. Grisogono, et al., *Rev. Geophys.* **53**, 956 (2015).
- [30] S. S. Zilitinkevich, T. Elperin, N. Kleeorin, V. L'vov and I. Rogachevskii, *Boundary-Layer Meteorol.* **133**, 139 (2009).
- [31] N. Kleeorin, I. Rogachevskii, I. A. Soustova, Yu. I. Troitskaya, O. S. Ermakova, S. S. Zilitinkevich, *ArXiv: 1812.10059* (2018).
- [32] S. S. Zilitinkevich, T. Elperin, N. Kleeorin and I. Rogachevskii, *Boundary-Layer Meteorol.* **125**, 167 (2007).
- [33] S. S. Zilitinkevich, T. Elperin, N. Kleeorin, I. Rogachevskii, I. Esau, T. Mauritsen and M. Miles, *Quart. J. Roy. Meteorol. Soc.* **134**, 793 (2008).
- [34] S. S. Zilitinkevich, I. Esau, N. Kleeorin, I. Rogachevskii and R. D. Kouznetsov, *Boundary-Layer Meteorol.* **135**, 505 (2010).
- [35] S. S. Zilitinkevich, T. Elperin, N. Kleeorin, I. Rogachevskii, and I. Esau, *Boundary-Layer Meteorol.* **146**, 341 (2013).
- [36] S. Toppaladoddi, S. Succi, and J. S. Wettlaufer, *Phys. Rev. Lett.* **118**, 074503 (2017).
- [37] J. Niemela, L. Skrbek, K. R. Sreenivasan, and R. J. Donnelly, *Nature (London)* **404**, 837 (2000).
- [38] P. G. Baines, *Topographic effects in stratified flows* (Cambridge University Press, New York, 1995).
- [39] R. E. Kelly, D. Pal, *J. Fluid Mech.* **86**, 433 (1978).
- [40] G. Seiden, S. Weiss, J. McCoy, W. Pessch, E. Bodenschatz, *Phys. Rev. Lett.* **101**, 214503 (2008).
- [41] S. Weiss, G. Seiden, E. Bodenschatz, *New J. Phys.* **14**, 053010 (2012).
- [42] S. Weiss, G. Seiden, E. Bodenschatz, *J. Fluid Mech.* **756**, 293 (2014).
- [43] G. Freund, W. Pesch, W. Zimmermann, *J. Fluid Mech.* **673**, 318 (2011).
- [44] X. Zhu, R. J. A. M. Stevens, R. Verzicco, D. Lohse, *Phys. Rev. Lett.* **119**, 154501 (2017).
- [45] P.-E. Roche, B. Castaing, B. Chabaud, and B. Hébral, *Phys. Rev. E* **63**, 045303 (2001).
- [46] G. Stringano, G. Pascazio, and R. Verzicco, *J. Fluid Mech.* **557**, 307 (2006).
- [47] R. H. Kraichnan, *Phys. Fluids* **5**, 1374 (1962).
- [48] S. Grossmann and D. Lohse, *Phys. Fluids* **23**, 045108 (2011).

- [49] S. Weinberg, Phys. Rev. **126**, 1899 (1962).
- [50] L. D. Landau and E. M. Lifshitz, *Quantum Mechanics: Non-Relativistic Theory*, Vol. **3** (Elsevier, Chicago, 2013).
- [51] R. J. Adrian, Annu. Rev. Fluid Mech. **23**, 261 (1991).
- [52] M. Raffel, C. Willert, S. Werely and J. Kompenhans, *Particle Image Velocimetry* (Springer, Berlin-Heidelberg, 2007).
- [53] J. Westerweel, Experim. Fluids **29**, S3 (2000).
- [54] A. Eidelman, T. Elperin, N. Kleeorin, A. Markovich and I. Rogachevskii, Experim. Fluids **40**, 723 (2006).
- [55] M. Bukai, A. Eidelman, T. Elperin, N. Kleeorin, I. Rogachevskii and I. Sapir-Katiraie, Phys. Rev. E **79**, 066302 (2009).
- [56] M. Bukai, A. Eidelman, T. Elperin, N. Kleeorin, I. Rogachevskii and I. Sapir-Katiraie, Phys. Rev. E **83**, 036302 (2011).
- [57] A. Eidelman, T. Elperin, I. Gluzman, N. Kleeorin and I. Rogachevskii, Phys. Fluids **25**, 015111 (2013).